PROCEEDINGS OF SPIE

Infrared Technology and Applications XXXIX

Bjørn F. Andresen
Gabor F. Fulop
Charles M. Hanson
Paul R. Norton
Editors

29 April–3 May 2013
Baltimore, Maryland, United States

Sponsored and Published by
SPIE

Part One of Two Parts

Volume 8704

Proceedings of SPIE 0277-786X, V. 8704

SPIE is an international society advancing an interdisciplinary approach to the science and application of light.

Infrared Technology and Applications XXXIX, edited by Bjørn F. Andresen, Gabor F. Fulop, Charles M. Hanson, Paul R. Norton, Proc. of SPIE Vol. 8704, 870401 · © 2013 SPIE
CCC code: 0277-786X/13/$18 · doi: 10.1117/12.2031913

The papers included in this volume were part of the technical conference cited on the cover and title page. Papers were selected and subject to review by the editors and conference program committee. Some conference presentations may not be available for publication. The papers published in these proceedings reflect the work and thoughts of the authors and are published herein as submitted. The publisher is not responsible for the validity of the information or for any outcomes resulting from reliance thereon.

Please use the following format to cite material from this book:
Author(s), "Title of Paper," in *Infrared Technology and Applications XXXIX*, edited by Bjørn F. Andresen, Gabor F. Fulop, Charles M. Hanson, Paul R. Norton, Proceedings of SPIE Vol. 8704 (SPIE, Bellingham, WA, 2013) Article CID Number.

ISSN: 0277-786X
ISBN: 9780819494955

Published by
SPIE
P.O. Box 10, Bellingham, Washington 98227-0010 USA
Telephone +1 360 676 3290 (Pacific Time) · Fax +1 360 647 1445
SPIE.org

Printed in the United States of America.

Publication of record for individual papers is online in the SPIE Digital Library.

SPIEDigitalLibrary.org

Paper Numbering: Proceedings of SPIE follow an e-First publication model, with papers published first online and then in print and on CD-ROM. Papers are published as they are submitted and meet publication criteria. A unique, consistent, permanent citation identifier (CID) number is assigned to each article at the time of the first publication. Utilization of CIDs allows articles to be fully citable as soon as they are published online, and connects the same identifier to all online, print, and electronic versions of the publication. SPIE uses a six-digit CID article numbering system in which:

- The first four digits correspond to the SPIE volume number.
- The last two digits indicate publication order within the volume using a Base 36 numbering system employing both numerals and letters. These two-number sets start with 00, 01, 02, 03, 04, 05, 06, 07, 08, 09, 0A, 0B … 0Z, followed by 10-1Z, 20-2Z, etc.

The CID Number appears on each page of the manuscript. The complete citation is used on the first page, and an abbreviated version on subsequent pages. Numbers in the index correspond to the last two digits of the six-digit CID Number.

Contents

Part One

Part 2

Conference Committee

Symposium Chair

Kenneth R. Israel, Major General (USAF Retired) (United States)

Symposium Cochair

David A. Whelan, Boeing Defense, Space, and Security (United States)

Conference Chairs

Bjørn F. Andresen, Acktar Ltd. (Israel)
Gabor F. Fulop, Maxtech International, Inc. (United States)
Charles M. Hanson, Texas Instruments Inc. (United States)
Paul R. Norton, U.S. Army Night Vision & Electronic Sensors Directorate (United States)

Conference Program Committee

Tayfun Akin, Middle East Technical University (Turkey)
Christopher C. Alexay, StingRay Optics, LLC (United States)
Jagmohan Bajaj, Teledyne Imaging Sensors (United States)
Stefan T. Baur, Raytheon Vision Systems (United States)
Philippe F. Bois, Thales Research & Technology (France)
Wolfgang A. Cabanski, AIM INFRAROT-MODULE GmbH (Germany)
John T. Caulfield, Cyan Systems (United States)
John W. Devitt, Raytheon Vision Systems (United States)
Nibir K. Dhar, Defense Advanced Research Projects Agency (United States)
Michael T. Eismann, Air Force Research Laboratory (United States)
Mark E. Greiner, L-3 Communications Cincinnati Electronics (United States)
Sarath D. Gunapala, Jet Propulsion Laboratory (United States)
Andrew Hood, FLIR Electro-Optical Components (United States)
Masafumi Kimata, Ritsumeikan University (Japan)
Hee Chul Lee, KAIST (Korea, Republic of)
Paul D. LeVan, Air Force Research Laboratory (United States)
Chuan C. Li, DRS Technologies, Inc. (United States)
Kevin C. Liddiard, Electro-optic Sensor Design (Australia)
Wei Lu, Shanghai Institute of Technical Physics (China)
Tara J. Martin, UTC Aerospace Systems (United States)
Paul L. McCarley, Air Force Research Laboratories (United States)
R. Kennedy McEwen, SELEX Galileo Infrared Ltd. (United Kingdom)
John L. Miller, FLIR Systems, Inc. (United States)

A. Fenner Milton, U.S. Army RDECOM CERDEC NVESD (United States)
Mario O. Münzberg, Cassidian Optronics GmbH (Germany)
Peter W. Norton, BAE Systems (United States)
Robert A. Owen, L-3 Communications Infrared Products (United States)
Joseph G. Pellegrino, U.S. Army Night Vision & Electronic Sensors Directorate (United States)
Ray Radebaugh, National Institute of Standards and Technology (United States)
Manijeh Razeghi, Northwestern University (United States)
Colin E. Reese, U.S. Army Night Vision & Electronic Sensors Directorate (United States)
Ingmar G. Renhorn, Swedish Defence Research Agency (Sweden)
Patrick Robert, ULIS (France)
Antoni Rogalski, Military University of Technology (Poland)
Ingo Rühlich, AIM INFRAROT-MODULE GmbH (Germany)
Piet B. W. Schwering, TNO Defence, Security and Safety (Netherlands)
Itay Shtrichman, SCD Semiconductor Devices (Israel)
Rengarajan Sudharsanan, Spectrolab, Inc., a Boeing Company (United States)
Stefan P. Svensson, U.S. Army Research Laboratory (United States)
Venkataraman Swaminathan, U.S. Army Armament Research, Development and Engineering Center (United States)
Simon Thibault, University Laval (Canada)
Gil A. Tidhar, Israel Aerospace Industries-ELTA (Israel)
Meimei Z. Tidrow, U.S. Army Night Vision & Electronic Sensors Directorate (United States)
Alexander Veprik, RICOR-Cryogenic & Vacuum Systems (Israel)
Jay N. Vizgaitis, U.S. Army Night Vision & Electronic Sensors Directorate (United States)
Michel Vuillermet, SOFRADIR (France)
James R. Waterman, U.S. Naval Research Laboratory (United States)
Lucy Zheng, Institute for Defense Analyses (United States)

Session Chairs

Opening Remarks
Bjørn F. Andresen, Acktar Ltd. (Israel)

1 NIR/SWIR FPAs and Applications
Tara J. Martin, UTC Aerospace Systems (United States)
Andrew Hood, FLIR Electro-Optical Components (United States)

2 Army Infrared R&D
Stefan P. Svensson, U.S. Army Research Laboratories (United States)
Mario O. Münzberg, Cassidian Optronics GmbH (Germany)
Gil A. Tidhar, Israel Aerospace Industries-Elta (Israel)

12 IR Optics II
Christopher C. Alexay, StingRay Optics, LLC (United States)
Jay N. Vizgaitis, U.S. Army Night Vision & Electronic Sensors Directorate (United States)
Troy A. Palmer, StingRay Optics, LLC (United States)

13 Active Imaging
Michael D. Jack, Raytheon Company (United States)
Ofer Nesher, Elbit Systems Ltd. (Israel)

14 HgCdTe
Joseph G. Pellegrino, U.S. Army Night Vision & Electronic Sensors Directorate (United States)
Gérard L. Destéfanis, CEA-LETI-Minatec (France)
Marion B. Reine, Photon Detector Physics, LLC (United States)

15 HgCdTe II
Joseph G. Pellegrino, U.S. Army Night Vision & Electronic Sensors Directorate (United States)
Gérard L. Destéfanis, CEA-LETI-Minatec (France)
Marion B. Reine, Photon Detector Physics, LLC (United States)

16 Smart Processing
Paul L. McCarley, Air Force Research Laboratory (United States)
John T. Caulfield, Cyan Systems (United States)
Paul R. Norton, U.S. Army Night Vision & Electronic Sensors Directorate (United States)

17 QWIP and Q-DOT
Henk Martijn, IRnova AB (Sweden)

18 Other Advanced Photon FPAs
Paul R. Norton, U.S. Army Night Vision & Electronic Sensors Directorate (United States)
Bjørn F. Andresen, Acktar Ltd. (Israel)

19 Emerging Uncooled Technologies II
Kevin C. Liddiard, Electro-optic Sensor Design (Australia)
John L. Miller, FLIR Systems, Inc. (United States)

20 Uncooled FPAs and Applications II
John L. Miller, FLIR Systems, Inc. (United States)
Kevin C. Liddiard, Electro-optic Sensor Design (Australia)

Introduction

The Thirty-Ninth conference on Infrared Technology and Applications was held the week of April 29th-May 3rd, 2013 at the Baltimore Convention Center in Baltimore, Maryland. The agenda was divided into 20 sessions:

1. NIR/SWIR FPAs and Applications
2. Army Infrared Research and Development I
3. Army Infrared Research and Development II
4. IR at Sea, in the Air, and in Space
5. IR in Future Soldiern Systems
6. Type II Superlattice FPAs I
7. Type II Superlattice FPAs II
8. Emerging Uncooled Technologies I
9. Uncooled FPAs and Applications I
10. HOT: High Operating Temperature FPAs
11. IR Optics I
12. IR Optics II
13. Active Imaging
14. HgCdTe FPAs and Applications
15. HgCdTe FPAs and Applications
16. Smart Processing
17. QWIP and Q-DOT
18. Other Advanced Photon PFAs
19. Emerging Uncooled Technologies II
20. Uncooled FPAs and Applications II

In addition, there were twenty-four poster papers presented for discussion on Thursday evening—these have been added to the 20 sessions in the Proceedings. Highlights of five topical areas are summarized below:

- Photon Detectors
- Uncooled Detectors
- Optics
- Smart Processing
- Applications

Photon Detectors

NIR/SWIR FPAs and Applications

Near-infrared and shortwave infrared imaging—0.7 to 3 μm—continues to rise in popularity because of its ability to make use of sky glow to enhance performance during exceptionally dark periods of the night. The primary technology being developed for these spectral bands is InGaAs, although other alternatives continue to be investigated. Session 1 addressed improvements in state-of-the-art InGaAs sensors, but it also addressed an alternative, silicon-based technology.

Dark current in SWIR detectors is inherently higher than that in detectors of visible light because the requisite bandgap for detection of SWIR radiation is somewhat smaller. Reduction of dark current is a continual pursuit for detectors in this spectral region as it is also in MWIR and LWIR photodetectors, because of the implications for cooling requirements. While those requirements are less stringent for SWIR detectors, they are nonetheless burdensome in terms of system power, especially when operation is required at elevated temperatures. One accepted means of reducing dark current is to form buried-junction diodes implanted at an InGaAs/InP interface, thus limiting the exposed surface area and the associated surface-generated dark current. Another means—illustrated in Fig. 1—has been developed that permits use of mesa diodes formed without the need for implantation, namely, the use of a graded InGaAlAs layer to transition from InGaAs to InAlAs. This process produced

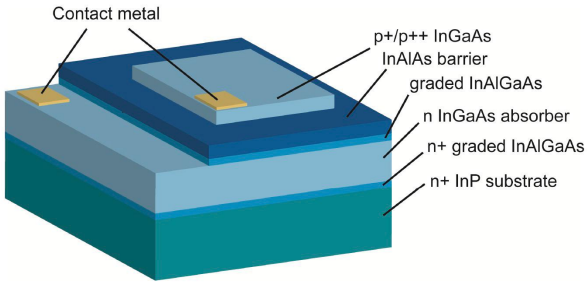

Fig. 1 Diagram of the epitaxial design and mesa structure for the epitaxially-passivated InGaAs mesa detectors.

devices that have areal dark current of 8 nA/cm^2 and perimeter dark current of 18 pA/cm, much of which was likely due to lateral collection in the unguarded diodes.

InGaAs arrays are now available in a number of configurations, including 320 × 256 with 30 µm pixels, 640 × 512 with 25 µm pixels, 640 × 512 with 12.5 µm pixels, and 1280 × 1024 with pixels as small as 15 µm. Dark currents are being reduced, but most devices still use thermoelectric coolers for operation at higher ambient temperatures. InGaAs material quality has been improved to the point that dark current is generally limited by interface effects, as evidenced by its dependence on the perimeter of a pixel rather than its area.

Some 1280 × 1024 arrays can operate at up to 50 Hz frame rates using only 2 outputs, and at higher frame rates with more outputs. In some cases the signal is handled by a charge-sensitive transimpedance amplifier having a photocurrent threshold above which the signal is logarithmically compressed, providing greatly extended dynamic range. In another variation the thermoelectric cooler (TEC) has been eliminated by characterizing the FPA over the range of operating temperatures and applying corrections accordingly. This, of course, does not reduce the impact of dark current on noise and dynamic range, but it does provide a sensor with significant capability at greatly reduced power, exchanging up to 6.5 W of TEC power for about 250 mW of processing power, giving a total system power of about 3.75 W across the temperature range.

Advances in black silicon extend responsivity of silicon-based sensors out to about 1.2 µm. This extended quantum efficiency—XQE in Fig. 2—is sufficient

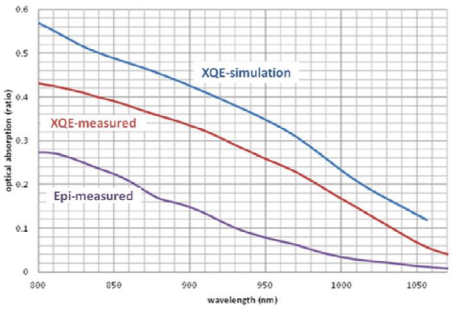

Fig. 2 Optical absorption spectra of thin silicon layers (<7 µm). XQE is enhanced by black silicon.

Fig. 3 Unassisted moonless night imaging collected using black silicon. The resolution of the sensor is 1280 × 1024 with an 10 µm pixel, the lens is F1.4 and captured at 30 fps.

to capture some of the sky-glow signal as well as to permit detection of 1064 nm lasers. The technology is positioned not as a substitute for InGaAs, whose response extends out to about 1.7 µm, but as a much lower cost alternative. Black silicon is formed by subpicosecond laser pulses that modify the structure and composition of the silicon surface. Use of this process does not affect the operation of standard silicon circuitry, enabling the monolithic use of standard CMOS processing, including those features that have made CMOS sensors performance-competitive with CCDs for most applications. Devices are fabricated on 8-inch wafers at the 180 nm process node, and pixels are 5.6 µm or 10 µm square. Figure 3 shows imagery on a moonless night with a light level below 5 mLux.

Type II Superlattice and Barrier FPAs

There were a total of eleven papers in the two sessions devoted to Type II Superlattice and Barrier detectors, and several more on this subject in the Poster session. This reflects the continued strong interest in the potential performance advantages that this technology has been predicted to have theoretically—long carrier lifetimes and a high optical absorption coefficient. Experimentally, lifetimes as long as those predicted have not yet been achieved, but improvements have been made recently for material structures that exclude gallium. Lifetimes continue to be shorter than for HgCdTe with comparable bandgaps.

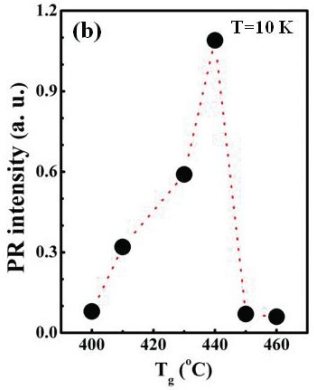

Fig. 4 Photoresponse intensity as a function of growth temperature (T_g).

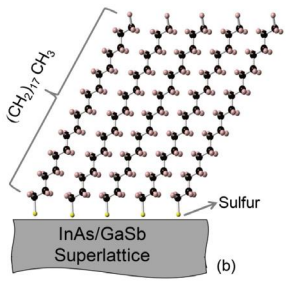

Fig. 5 Schematic of the sulphur molecule on the superlattice surface.

A comparison of detector performance for a series of superlattices grown with a bandgap of approximately 50 meV over a range of growth temperatures found that a growth temperature of 440 °C gave optimal photo-response as measured by photoconductivity. Fig. 4 illustrates this result.

Passivation of superlattice mesa sidewalls with sulfur atoms at the end of organic molecules was shown to lower the leakage current compared to unpassivated mesas. The surface configuration is shown in Fig. 5.

Defects and noise in Type II superlattice detectors were examined using synchrotron X-rays to characterize threading dislocations. The MWIR detectors were dominated by g-r dark current. For devices with noise values above that caused by g-r currents. A model—see Fig. 6—was suggested that avalanching occurs around localized crytallographic defects to explain the excess noise characteristics.

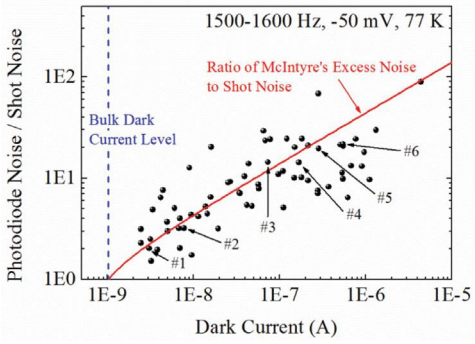

Fig. 6 Ratio of the measured photodiode noise I_n and the expected shot noise versus the dark current at a reverse bias of -50 mV for the set of 68 MWIR InAs/GaSb T2SL diodes. The bulk dark current level at -50 meV is marked by the dashed blue line. The solid red line shows the ratio of the excess noise according to an avalanche process to the expected shot noise.

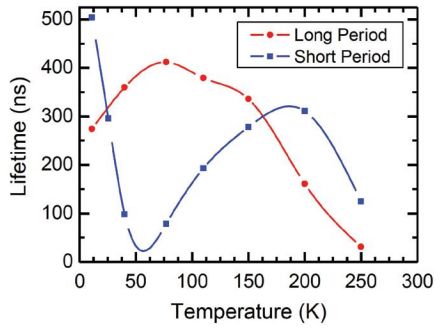

Fig. 7 Carrier lifetime of a long-period (red, circles) and a short-period (blue, squares) InAs/$InAs_{1-x}Sb_x$ T2SL.

Type II SLS lifetime was measured using time-resolved photoluminescence. Using a sub-bandgap laser to fill the recombination traps in a sample with an InAs/GaSb absorber, the lifetime was increased from about 30 nsec to 140 nsec—a value that may be indicative of radiative recombination. In another sample—see Fig. 7—that did not include Ga, the lifetime was as long as 400 nsec for long-period samples that had minimal overlap of the electron and hole wavefunctions.

Another paper reported on the comparison between unpassivated, Si_3N_4-passivated, and SiO_2-passivated MWIR Type II superlattice detectors. SiO_2 gave the lowest noise. Even so there was bias-dependent 1/f noise above 10 Hz as illustrated in Fig. 8.

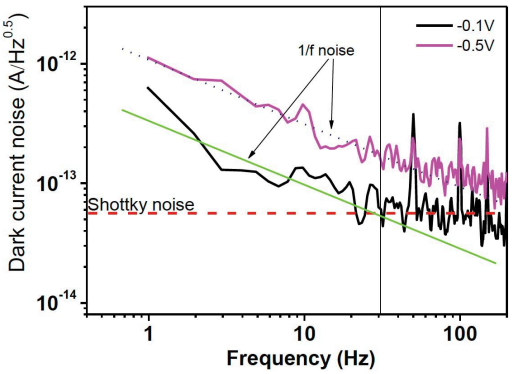

Fig. 8 Noise spectra as function of frequency for SiO_2 passivated devices at -0.1V and -0.5V (temperature 79K). The fitted strait line and dotted lines indicates the 1/f-noise behavior.

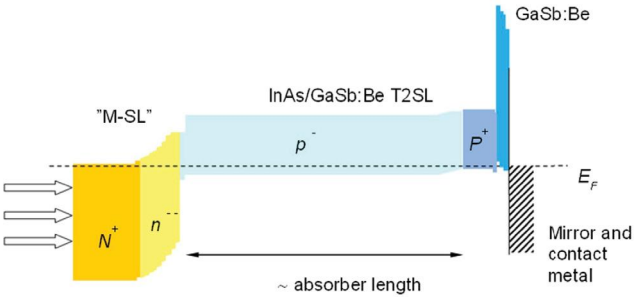

Fig. 9 Overview of the detector structure at zero bias.

An MWIR superlattice design that uses barriers to reduce g-r noise components was described. Fig. 9 illustrates the device design. Effective passivation and 65 % quantum efficiency were reported.

4-inch GaSb substrate development continues with a report on the implementation of polishing for these larger wafers. Fig. 10 shows a large GaSb crystal being pulled from a melt using the Czochralski method.

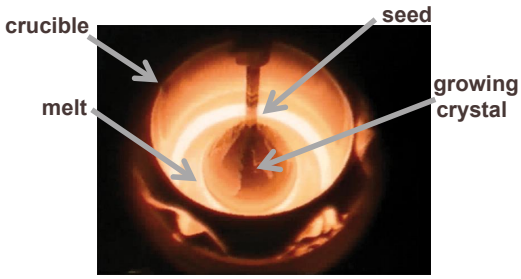

Fig. 10 A bulk GaSb crystal being grown by the Czochralski method.

Efforts continue to grow novel III-V detectors on non-lattice-matched substrates. Growth of a variety of *nBn* device designs on 6-inch GaAs substrates were made—see Fig. 11. The crystal and electrical properties were studied.

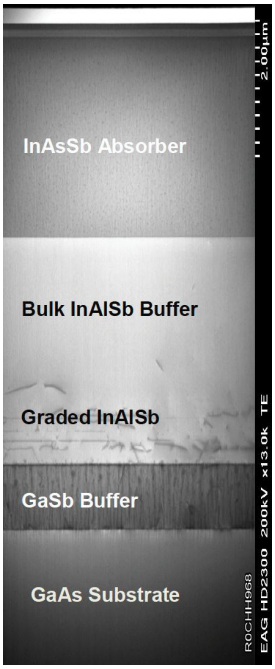

Fig. 11 One of the full nBn structures grown on a GaAs substrate

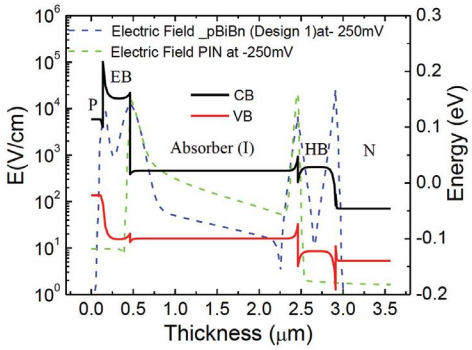

Fig. 12 Band structure of a *pBiBn* Type II superlattice and a comparison of the electric field in it to a conventional *pin* device at 250 mV reverse bias.

A *pBiBn* structure was reported to reduce dark current in a Type II superlattice-based low-noise LWIR photodetector. Fig. 12 shows the band structure of *pBiBn* design and compares electric field of that design to that of a *pin* diode design.

A thin intrinsic-layer Type II superlattice design with an "N" structure was described. This arrangement uses an AlSb barrier to aid in getting the electron and hole wave functions to overlap—see Fig. 13.

A variety of InAs superlattice layer thicknesses were grown in combination with a constant 7 mL GaSb thickness as part of a project to extend this technology to a 15 µm cutoff for space applications. Fig. 14 shows the spectral response of the samples measured at 3 K.

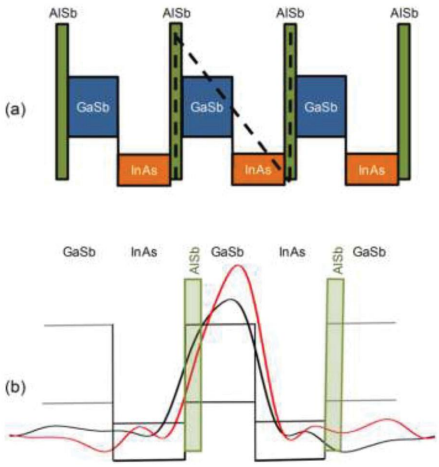

Fig. 13 (a) Conduction and valance band profiles for the proposed InAs/AlSb/GaSb based T2SL "N" structure. (b) Overlap integral for InAs/AlSb/GaSb based N-structure with AlSb barrier (red line) and Standard InAs/GaSb T2SL without AlSb barrier (black line) under 0.001meV bias. Negative bias is applied to the right side of the structure.

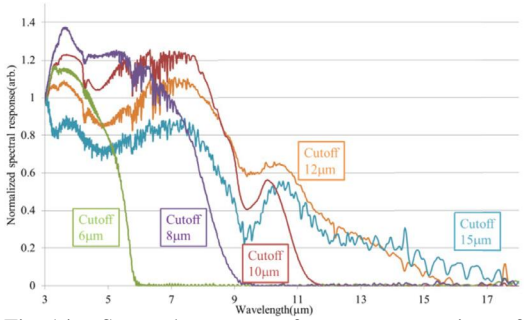

Fig. 14 Spectral response from a progression of superlattice samples grown with different InAs thickness and constant GaSb layers.

High Operating Temperature (HOT) FPAs

The goal of increasing the operating temperature of FPAs without sacrificing performance is motivated by the reduction in cooler power, improved cooler efficiency, longer cooler lifetime, smaller imager size, and lighter weight sensor systems that this makes possible. This goal is being pursued using HgCdTe, Type II superlattices, and *nBn* materials and has relevance especially in the MWIR and LWIR spectral bands.

An *nBn* FPA was described based upon an InAsSb absorber layer that is lattice matched to its GaSb substrate. This device operates only out to 4.2 μm which helps to provide higher operating temperature compared to arrays that extend closer to or beyond 5 μm. There is also an argument that the band short of the CO_2 atmospheric absorption between 4.2 and 4.3 μm can be less absorbing which helps at longer transmission distances. Fig. 15 shows how the signal-to-noise

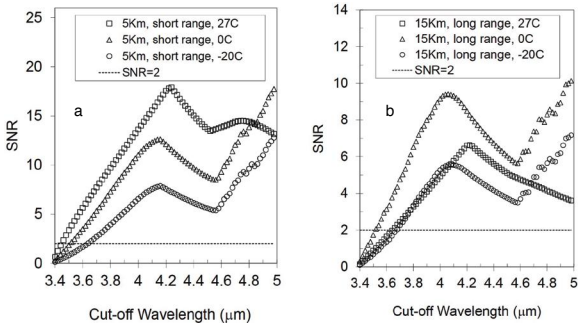

Fig. 15 SNR versus cutoff for (a) a short range hand held system looking at scenery 5 Km away and (b) a long range observation system looking at scenery 15 Km away. For each system, 3 environmental temperatures are tested (-20°C, 0°C and 27°C) where a temperature contrast of 1°C in the landscape is assumed. In each plot, the dashed line indicates SNR=2, which is taken to be the threshold for a meaningful image.

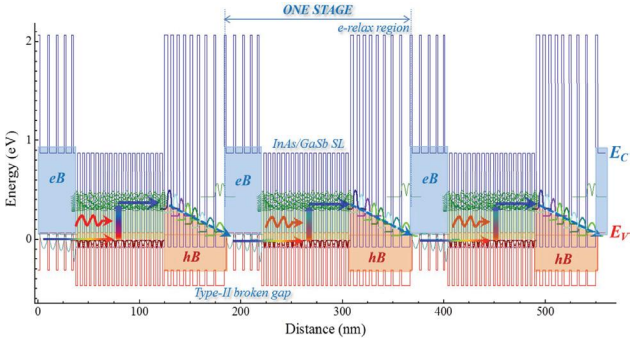

Fig. 16 Band diagram of a modified mid-IR interband cascade photodetector—the envelop wave-functions and their energy levels are shown. The incoming photons are absorbed in the InAs/GaSb SL absorber, generating electron-hole pairs. The electrons will diffuse into the electron relaxation region, and then effectively transport into the valence band of the next stage, through fast LO-phonon assist intraband relaxation and interband tunneling.

ratio (SNR) varies with cutoff for range distances of 5 and 15 km and for three scene temperatures. The sacrifice for the shorter waveband is that it requires longer integration times to half-fill the unit cell integration capacitor—16 msec at f/4—and that penalty increases with decreasing scene temperature.

Another paper reported on HOT nBn operation with an interband cascade structure—see Fig. 16—that has multiple absorber regions sandwiched between barriers. Separation of electrons and holes in the structure provides a photovoltaic-like response. The measured device had a cutoff (50 %) of about 3.8 μm at 80 K which increased to about 4.3 μm at 300 K. Operation was reported for temperatures as high as 420 K.

Photon-trapping was included in another HOT paper that used an *nCBn* structure with an InAsSb absorber with a 5.2 μm cutoff at 200 K. Fig. 17 shows a cross-sectional schematic and an SEM photo of the

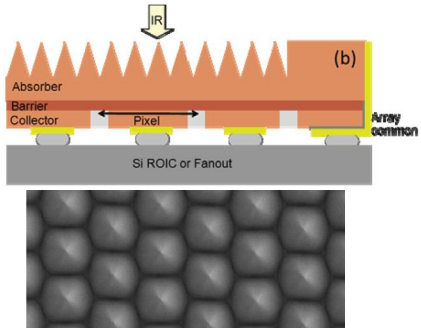

Fig. 17 Detector cross-section with pyramidal absorber (top); SEM pictures of staggered pyramids (bottom)

Fig. 18 MWIR, and SWIR image at 81 K of a student holding a 3.69 μm narrow-band optical filter in front of a heat gun.

staggered pyramid "traps". Compared to side-by-side arrays without the pyramid absorbers, the dark current was reduced by a factor of ~3 with the pyramids.

A dual-band Type II superlattice focal plane was reported that combined SWIR—2 μm—and MWIR—4.2 μm—bands. This combination is able to image in both reflective and emissive bands that are not highly correlated. Fig 18 shows imagery from both bands. Substrate removal was used to allow full sensitivity of the SWIR band.

An *nBn* HOT modeling paper considered InAsSb/AlAsSb MWIR device structures and results were presented for dark current, barrier dependence on bias, quantum efficiency, photocurrent, spectral responsivity, D*, and R_0A product. A comparison was made between *nBn*, and p-on-n diodes—both InAsSb and HgCdTe. Figure 19 shows that particular comparison.

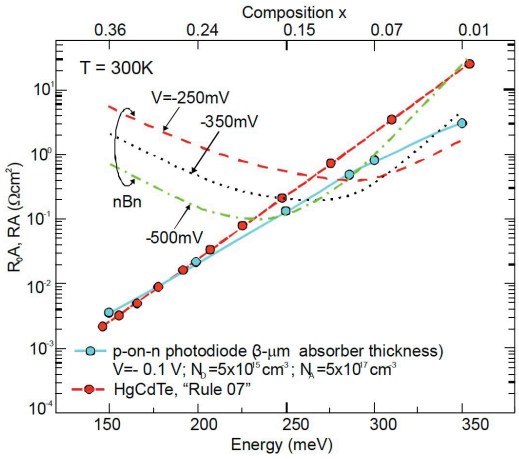

Fig. 19 R_0A and RA product of MWIR InAsSb/AlAsSb *nBn* detector and p-on-n InAsSb photodiode versus InAsSb absorption layer gap energy. R_0A is calculated in accordance with HgCdTe "Rule 07".

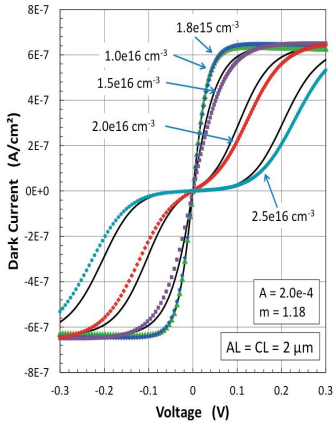

Fig. 20 Simulations for dark current density for nBn detectors, for a range of donor concentrations in the n-type BL.

The second modeling paper focused on conditions of doping and bias that allow an *nBn* detector to operate in a region that is free of depletion regions. Both n-type and p-type barriers were considered. The dark current was calculated for a range of bias voltages with the doping concentration of the barrier as a parameter as illustrated in Fig. 20.

The session ended with a presentation on enhancing HOT performance by reducing the volume of the detector material while retaining high quantum efficiency. Fig. 21 shows an SEM photo of the device structure with etched holes where material has been removed. Efficient internal reflection allows all of the light to still be absorbed in the remaining material. The approach has been applied to dual-band designs.

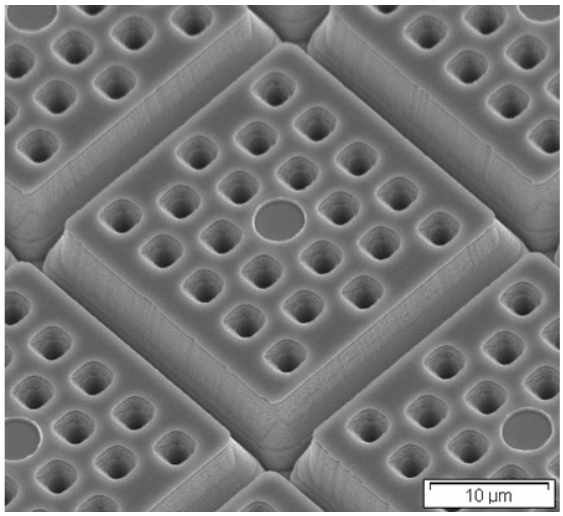

Fig. 21 Photon trapping dual-band SWIR/MWIR detector design.

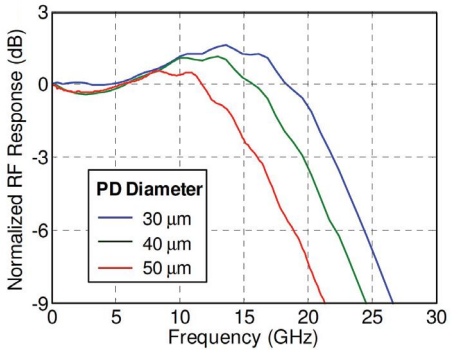

Fig. 22 Normalized RF response for 30 µm, 40 µm, and 50 µm diameter photodiodes having internal 50 Ω termination at 5 V reverse bias.

Active Imaging

Active imaging is based upon the combination of laser illumination and fast, SWIR, avalanche photodiode (APD) arrays that can extend recognition ranges with the higher resolution available with shorter wavelengths.

A very high speed (up to 25 GHz) InGaAs diode with a 2.2 µm cutoff was reported that has very high photocurrent capacity allowing it to utilize high local oscillator power with minimal signal compression. Fig. 22 shows the frequency response for three diode sizes.

A variety of InGaAs absorbers coupled with an InAlAs avalanche region APDs were reported with k < 0.15. Fig. 23 shows the device current in the dark and with illumination.

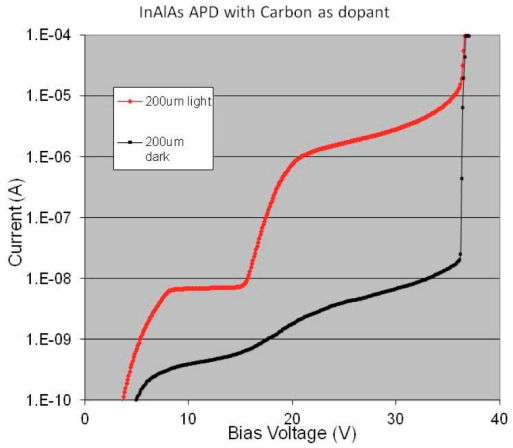

Fig. 23 Current voltage characteristics for a 200 µm diameter InAlAs APD with carbon as a dopant.

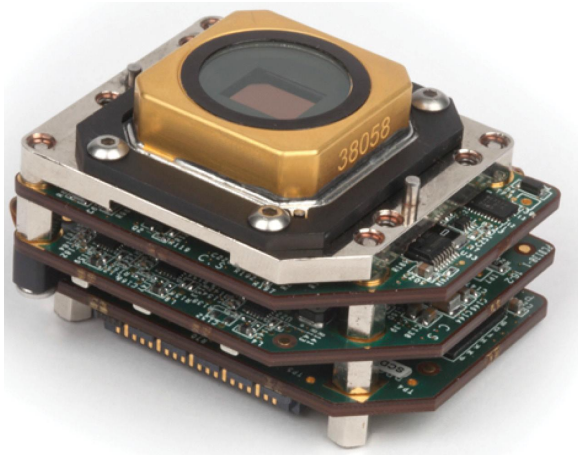

Fig. 24 Photo of the InGaAs detector including the proximity electronic boards.

A multi-function readout combined with an InGaAs SWIR array with 15 µm pitch was described having high- and low-gain and asynchronous laser pulse detection. Fig. 24 is a photograph of the sensor package together with proximity electronics. Sensitivity can be extended into the visible spectrum with optional substrate removal.

Human identification at long range was the subject of an active-SWIR paper. Fig. 25 illustrates the system concept.

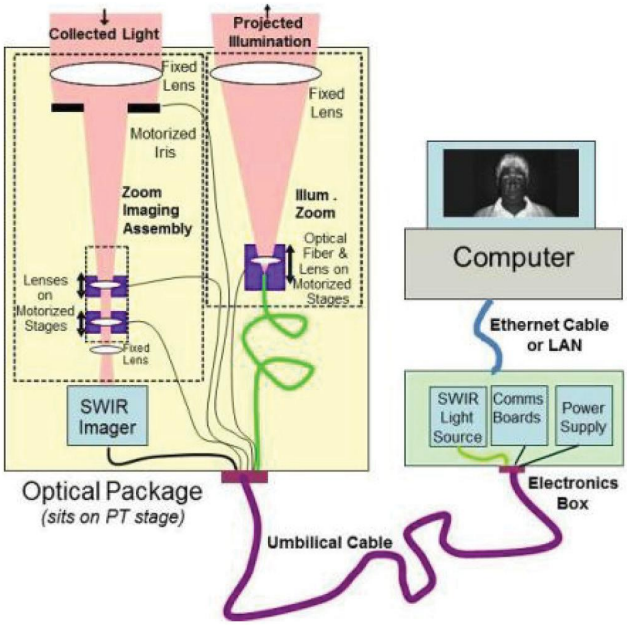

Fig. 25 Conceptual illustration of the long-range, active SWIR facial recognition hardware.

The HgCdTe alloy detector—characterized by a high absorption coefficient and a long lifetime—continues to dominate the choice for a broad range of infrared applications. Aside from applications that are ideal for either InSb in the MWIR spectral band, or InGaAs in the 1.7 μm SWIR band, or those that can utilize uncooled FPAs, HgCdTe continues to be the most popular choice. Papers in this section update how HgCdTe is continuing to develop and evolve. Papers on this topic were presented in two sessions on HgCdTe detectors as well as in the HOT session, the Applications sessions, and in the Poster session.

Development of large format MWIR and LWIR detectors for a 1280 × 1024 format with 15 μm pixels was described using both LPE on CdZnTe substrates and MBE on GaAs substrates. Fig. 26 is an example of an image taken with an LWIR array fabricated from MBE-grown material.

Very large format, 1960 × 1080 arrays with 12 μm pixels of MWIR HgCdTe grown by MOVPE on GaAs were reported. These FPAs are 3-side buttable—the FPAs can be spaced closely together on 3 sides of each array. A mosaic of 8 FPAs using this approach is shown in Fig. 27 giving a total of 16 Mpixels.

Fig. 26 LWIR image from an MBE-grown HgCdTe array of 1280 × 1024 pixels with 15 μm pitch at 76 K. This array has a cutoff of 8.8 μm at 80K.

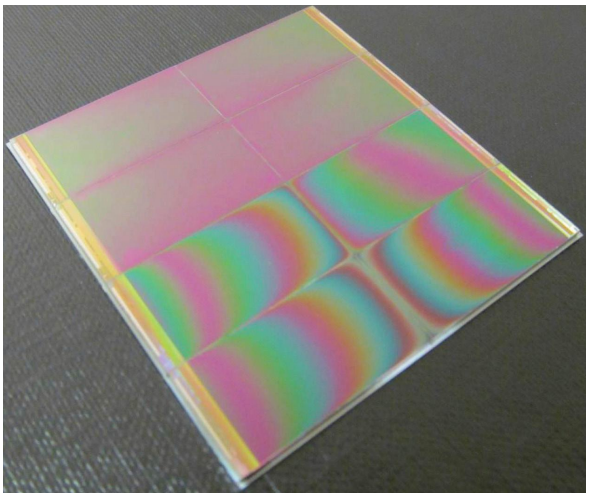

Fig. 27 16 Mpixel MWIR mosaic array using eight 1960 × 1080 arrays with 12 μm pixels. Four devices have different AR coating.

Progress in HgCdTe across a broad range of material technologies, devices, and applications was reported. CdZnTe substrates with diameters as large as 115 mm were shown. Devices with both n-on-p and p-on-n are being utilized with success. Applications including avalanche photodiodes and VLWIR arrays for space applications. Pixel pitch reduction down to 10 μm and less is being accompanied by plans for the development of larger formats—1024 × 768 and 2K × 2K. Dark current is reduced by two orders of magnitude with newer p-on-n diodes, including in the SWIR band. Fig. 28 shows a roadmap for dual band detector development.

The temperature dependence of 1/f noise was studied for both MWIR and LWIR n-on-p detectors. Fig. 29 shows how the main distribution and the high-noise tail for an MWIR array vary with temperature be-

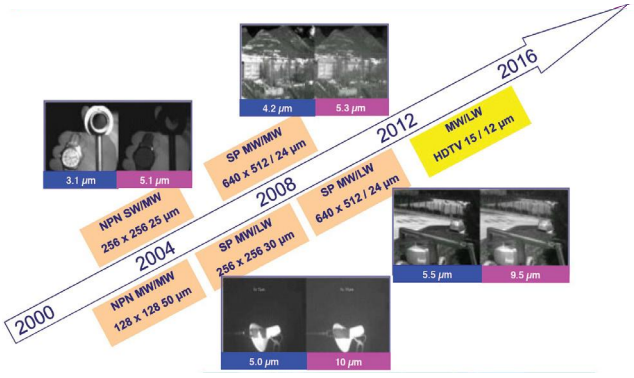

Fig. 28 Roadmap for dual-band detector development.

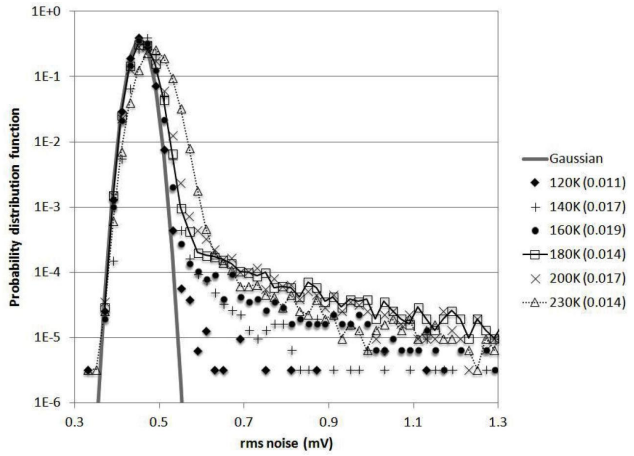

Fig. 30 Temperature dependence and nonparametric skew of the rms noise probability distribution function for a single 640 × 480 MWIR array integrated to 50 % full well condition, showing that the peak broadens with increasing temperature but the magnitude of the tail saturates at 180 K.

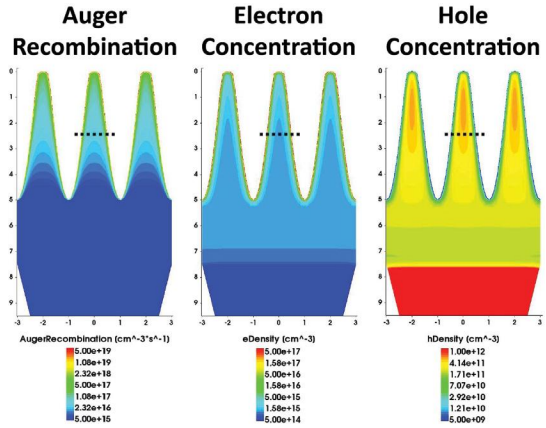

Fig. 31 Auger recombination (left), electron density (center) and hole density (right) for the center pixel are shown by performing a linecut through the center of the array. In these plots the surface recombination velocity is 1000 cms^{-1}, the surface charge is 10^{12} cm^{-2} and the array is illuminated with planewaves at $\lambda = 1.0$ μm.

tween 120 and 230 K. A temperature dependence proportional to n_i was observed for standard FPAs.

VLWIR HgCdTe detectors are being developed with p-on-n technology as described by one paper. Fig. 30 shows how the R_0A product of this technology compares with other reports in the literature and a heuristic equation that describes the state-of-the-art for this technology.

A finite-difference, time-domain model was used to calculate the quantum efficiency and surface recombination in HgCdTe photonic trapping structures. Fig. 31 illustrate the results of one of the model runs.

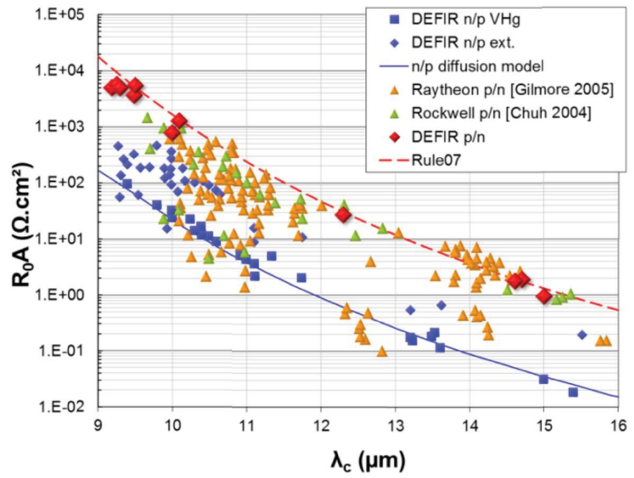

Fig. 30 R_0A data as a function of detector cutoff wavelength for pn diodes compared with np diodes with Rule 07 for reference.

A multispectral camera—an array of filters over 256 × 320 array of MWIR HgCdTe detectors—was used to monitor the spectral composition of a burning propellant. Fig. 32 shows the arrangement of the filters that gave 11 MWIR spectral channels and the spectral coverage of each.

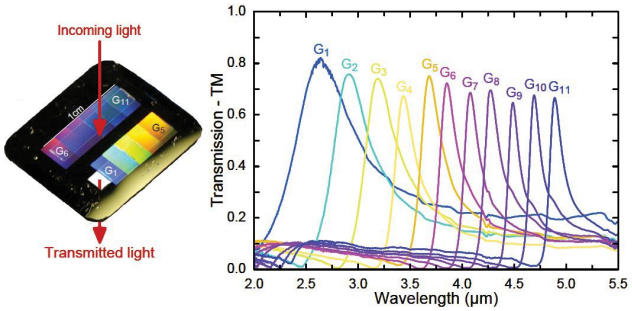

Fig. 32 (left) Overview of the filter arrays. Eleven filters are free-standing and one path is filter-free for wide-band imaging. (b) Transmission spectra of the filters measured with a Fourier-transform infrared spectrometer under normal incidence and for TM-polarized wave.

QWIP and Q-Dot FPAs

Quantum dot structures were discussed in four papers at the conference. In the first of these, Type II In(Ga)Sb superlattice dots were embedded in an InAs matrix. Fig. 33 illustrates one of the structures that was fabricated and measured—an LWIR *pin* diode.

Quantum dot LWIR detectors were characterized as a function of temperature for devices that had a pho-

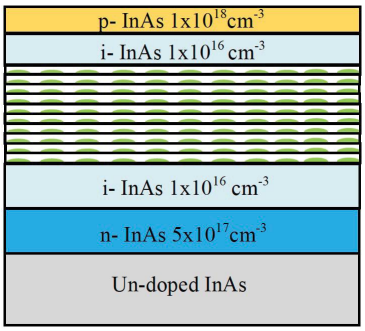

Fig. 33 Quantum dot-to-band detector structure with 10 QD layers separated by InAs spacer in a pin polarity.

torespsonse based upon an indirect bandgap. Fig. 34 shows how thermal activation can play a role in enabling the photoresponse in this case.

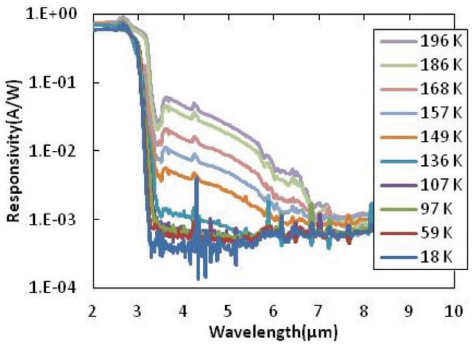

Fig. 34 Photoresponse spectra at different temperatures from a quantum dot detector with a spatially-indirect activation path.

A reduction by five orders of magnitude in the dark current of an InGaAs/GaAs quantum dot device following ion implantation was reported.

The novel use of PbS quantum dots in a hetro-structure with electron- and hole-blocking layers—see Fig. 35—was described. The device can be deposited directly onto a silicon readout.

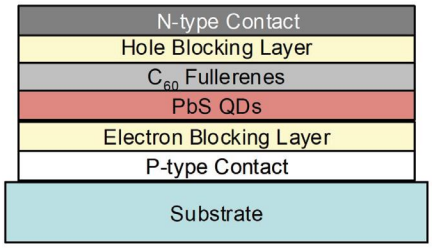

Fig. 35 This quantum dot device is based on PbS-C_{60} heterojunction that provides efficient charge separation and carrier extraction.

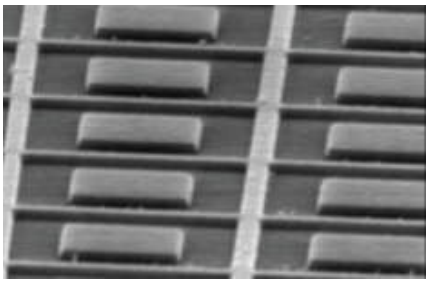

Fig. 36 The backside of a QWIP array is patterned with a metamaterial pattern with the aid of e-beam photolithography.

Other Advanced Photon FPAs

The use of broadband resonators to enhance the absorption in infrared detectors was proposed. Fig. 36 shows an array of such resonators fabricated by e-beam lithography in conjunction with a QWIP detector array. The use of these metamaterials was suggested for use in infrared sensors capable of "color" imaging.

The development of a 1920 × 1536 pixel InSb array having 10 μm pixels with operation up to 120 Hz was described. On-chip analog-to-digital conversion is provided by 3840 A/Ds—one at the top and bottom of each array column. An image taken with this array is shown in Fig. 37.

SiGe technology for low-cost SWIR sensors was the subject of the final presentation of this session. Low-cost is implied by the fact that SiGe technology can be

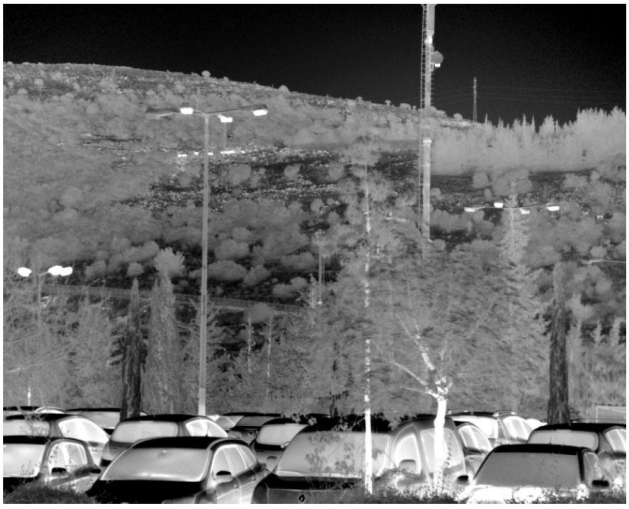

Fig. 37 Image from a 1920 × 1536 pixel InSb array having 10 μm pixels at F/3.

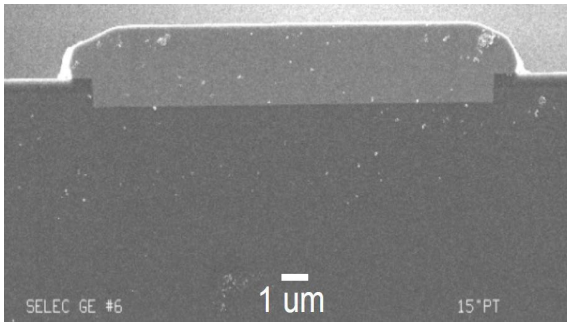

Fig. 38 Scanning electron microscope image of the cross-section of a selective-epitaxial grown region of Ge-on-Si test structure.

processed on 12-inch silicon wafers using selective-area epitaxy—see Fig. 38.

Uncooled Detectors

Emerging Uncooled I & II

In addition to progress in the development of bolometers and bolometer-like uncooled detectors, new ideas continue to emerge. Presentations included novel detector materials, variations in pixel design, innovative absorption methods, new detection techniques.

Plasmonic absorbers formed by a rectangular array of cylindrical dimples in a gold film have been shown to provide high narrow-band absorption in the MWIR and LWIR for MEMS-based IR detectors. The absorption peak is determined by the spacing of the dimples. The full width, half maximum for the absorption peak is typically 80 nm, and absorption outside of that region is generally in the 20% to 40% range, as shown in Fig. 39. This enables the fabrication of detector arrays in which all pixels experience the exact same process, but different pixels can have different spectral sensitivities, even so far as being sensitive to different spectral bands.

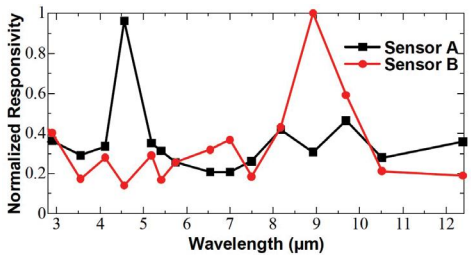

Fig. 39 Measured spectral responsivities for sensors with (A) and without (B) a plasmonic absorber.

Another means of customizing the absorption spectrum is the use of a frequency-selective surface (FSS). Both resistive dipoles and slots in a resistive sheet, both shown in Figure 40, provide relatively narrow-band absorption. The former transmits most out-of-band radiation, whereas the latter reflects it. This permits a dual-band sensor as shown in Fig. 41, wherein the top layer absorbs MWIR and transmits LWIR, and the second layer absorbs LWIR and reflects MWIR. Thus, the second layer serves as the mirror for the upper (MWIR) resonant cavity, while also serving as the absorber for the lower (LWIR) resonant cavity. The resulting absorption spectrum is shown is Fig. 42.

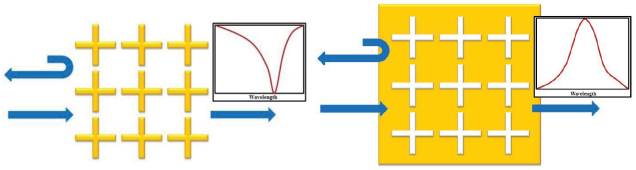

Fig. 40 Characteristics of patterned resistive sheets. Out-of-band transmission characteristic of dipole patterned (left). Out-of-band reflection characteristic of slot patterned (right).

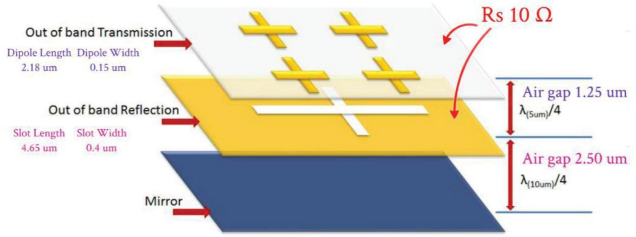

Fig. 41 Dipole-Slot-Mirror stacked structure for improved power absorption efficiency

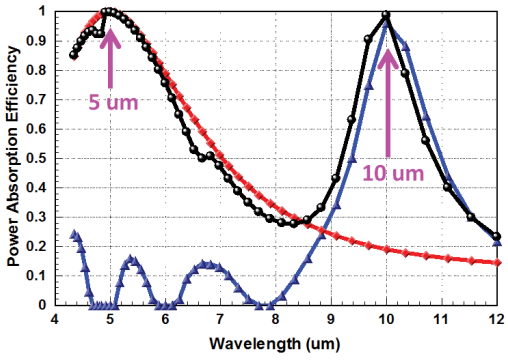

Fig. 42 Absorption peaks between optimized dipole-slot stack layer and each individual layer

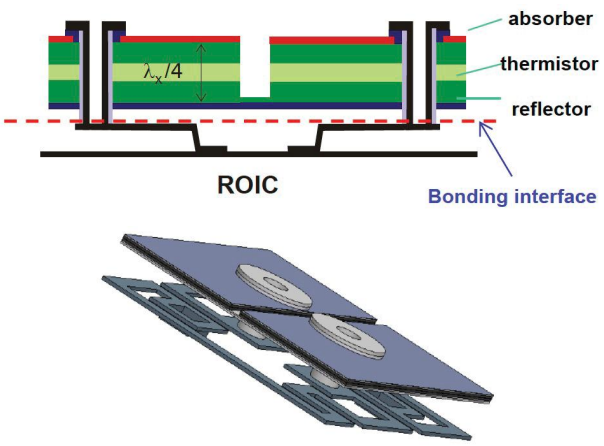

Fig. 43 Schematic representations—cross section top, 3D bottom—of the quantum well bolometer pixel illustrating the electrical connections to the underlying ROIC via the supporting legs.

Among the approaches for improvement of bolometer arrays is the use of Si/SiGe quantum wells as the sensitive material. The material must be processed at temperatures higher than those a standard CMOS circuit can withstand, so the device is prepared with a film-transfer process. The pixel is designed as shown in Fig. 43 so that current flows transversely through the multiple layers of the quantum well, and the top electrode is split to allow for a double pass. The advantages claimed for this approach are higher TCR and reduced 1/f noise.

Novel concepts in the early stages of development included an optical resonator whose resonance is spoiled by a change in temperature, and an electrically activated cantilever for which deformation due to a temperature change causes a variation in the time required for the cantilever to relax and make contact with an electrode, the signal being a digital representation of that time.

Uncooled I and II

The uncooled session started with a memorial tribute to Paul Kruse—right—who was one of the pioneers not only in uncooled detector technology but also in cooled infrared detectors.

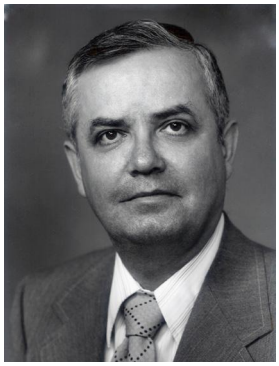

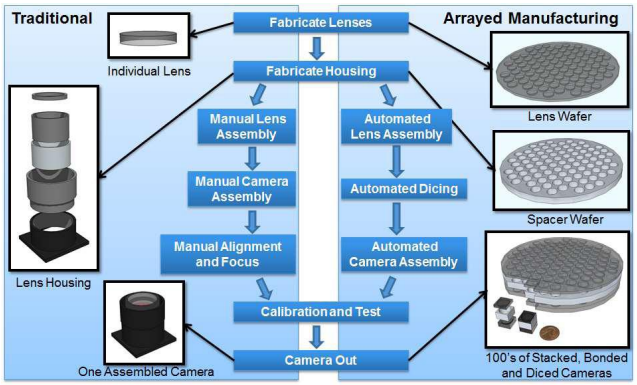

Fig. 44 Arrayed vs. Traditional Manufacturing of uncooled FPAs.

The two leading uncooled technologies – vanadium oxide (VO_x) and amorphous silicon microbolometers continue to advance although there were no papers reporting on the latter technology.

VO_x microbolometers with 17-µm pixel pitch are now widely available. Sub-17-µm pitch FPAs are under development.

One company compared the performance of its 1024 × 768 pixel VO_x microbolometer with 17-µm pitch to that of a cooled 2nd Gen sight (288 × 4 HgCdTe with TDI scanning) in a simulation and found that the uncooled sight had better range performance than the cooled sight.

An overview was given of development of sub-17-µm 640 × 480 VO_x arrays with wafer-scale optics, electronics and vacuum packaging. Fig. 44 shows the manufacturing process for Arrayed Manufacturing vs. Traditional Manufacturing.

Some groups are experimenting with combinations of vanadium oxide with other metals.

A Japanese company described their 640 × 480 microbolometer with 12 µm pitch that was made using vanadium niobium oxide as the bolometric material. The addition of Nb to VO_x resulted in a TCR of -3.6%/K. In addition, the thermal isolation was improved by a factor of five to 5 nW/K by using a three-level structure—see Fig. 45. The resulting FPA had an NEΔT of 60 mK @f/1 and 30 Hz. Images from a miniature camera are shown in Fig. 46.

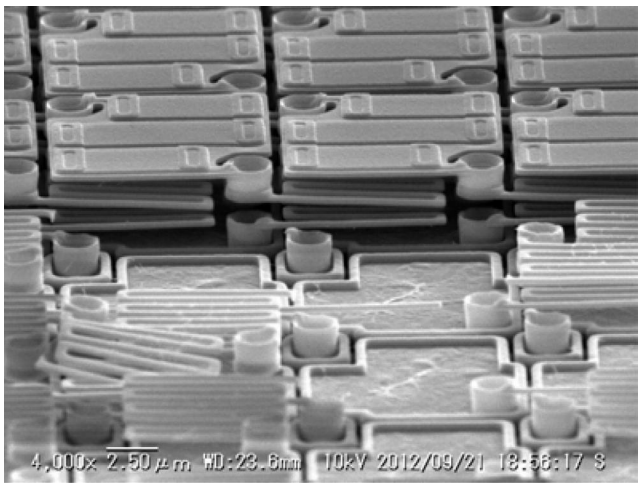

Fig. 45 Three-level pixel structure with 12 μm pitch.

Fig. 46 Image from a 640 × 480 VO_x microbolometer with 12 μm pixels.

Researchers in South Korea have fabricated a small low-cost 32 × 32 microbolometer array with vanadium tungsten oxide. The array is intended to be used for measuring body temperature. The FPA is wafer-level vacuum packaged (WLVP) and has an an NEΔT of 100 mK.

A Japanese company has enhanced its SOI (silicon-on-insulator) uncooled FPA (320 × 240/22) by making its ROIC temperature independent using correlated double sampling (CDS) operation with reference pixels that are insensitive to infrared radiation. The resulting FPA requires no TE cooling between -30 and 80 ° C. The structure of a unit cell is shown in Fig. 47.

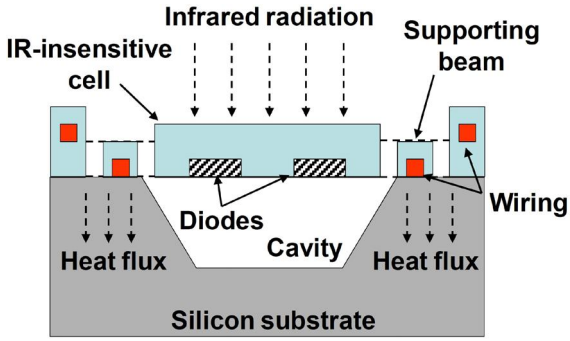

Fig. 47 SOI FPA with new reference pixel

Other uncooled papers included:

- An 80 × 80 PbSe array that is deposited by vapor phase deposition (VPD) directly on large CMOS wafers. The MWIR FPAs can be operated at full frame rates as high as 2 kHz.
- Pyroelectric arrays of relatively small formats—without MEMS processing and vacuum packaging—used for people counting and thermal imaging.

Optics

Several optics presentations discussed new optical materials, including coatings, and optical designs which are required in order to work with the new multiband infrared detectors and systems.

One company outlined a wide-angle catadioptric design combined with a method for selection of materials suitable for spanning a 0.6 – 11.0 μm wide band. Color correction was maximized, a flat field was provided to the FPA and a significantly reduced package size was achieved. The modular, compact design—Fig. 48—answers requirements for many applications

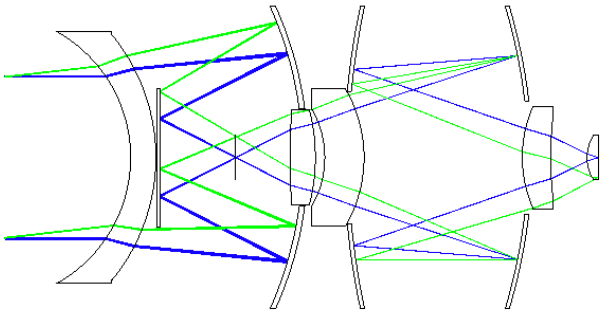

Fig. 48 Layout of 50 mm F/1, 0.6 –-11 μm catadioptric system.

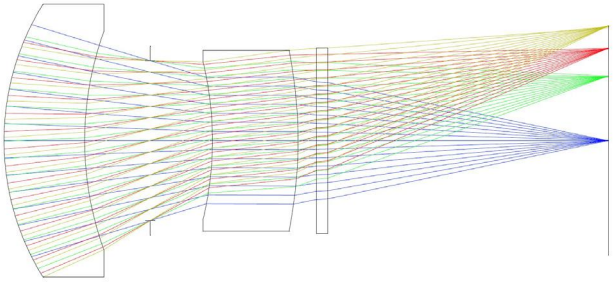

Fig. 49 A dual-band MWIR/LWIR optics design. The camera specifications include f/2.5, 51 mm focal length with a 220 diagonal full field of view (FOV).

such as helmet-mounted devices, hand-held devices and UAVs.

A government laboratory reported on their development of new IR glasses for applications covering all the SWIR + MWIR + LWIR wavebands. These new glasses in general have negative or very low dn/dT, making it easier to athermalize the imaging system. They offer some unique solutions for multiband achromats which can significantly reduce the size and weight of the imager for payload sensitive applications. Advantages of the new materials were demonstrated through preliminary design of a MWIR/LWIR multispectral imager—see Fig. 49.

Two presentations addressed anti-reflection optics coatings required for multi band IR systems. One company showed their dual-band and triple-band coatings for the 1.06 μm (YAG laser wavelength), 3-5 μm and 8-12 μm spectrum regions designed and deposited on ZnSe, ZnS, Ge and IG-6 substrates—see Fig. 50. The number of coating layers were restricted to 7-20

Another company presented a new technology – hybrid-Diamond-Like-Carbon (h-DLC) coating for multispectral optical systems. The technology combines the superior toughness of protective DLC coatings

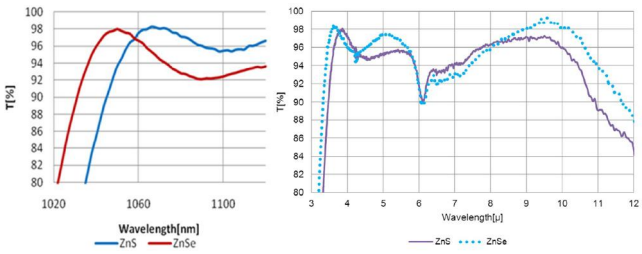

Fig. 50 Measured results of transmitance on ZnSe and Zns at normal incidence for a triple-band AR coating design.

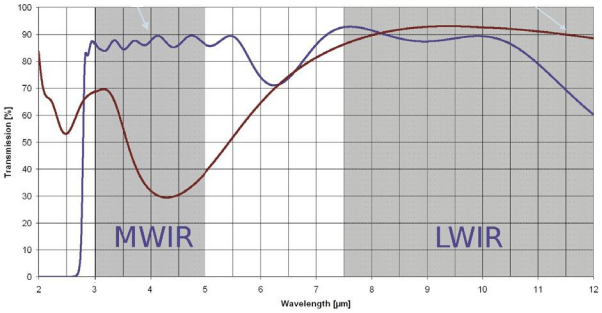

Fig. 51 Hybrid-DLC for dual band applications.

with the versatility and multispectral functionality of IR coatings. Figure 51 shows a comparison between h-DLC for a dual MWIR/LWIR coating (blue) and a DLC coating optimized for the LWIR band (red).

Ways of reducing cost of optical systems was one of the main subjects of the IR optics sessions. Can optical Performance (P) be optimized while at the same time minimizing Size (S), Weight (W) and Cost (C)?

One company discussed impact on optics SWaP-C (where P stands for Performance and not Power as in detector modules) by introduction of glass aspheres and molded polymer aspheres. The results of the discussion are summarized in Table I. The trade benefits of using polymers and moldable glasses in optical designs were demonstrated in two examples to reduce size, weight, and cost while maintaining high performance.

A team of scientists from industry and university laboratories outlined a combination of two approaches for reducing cost of uncooled IR imagers. The first approach consisted of developing new low-cost chalcogenide glasses with better mechanical properties than those presently available. New ways of fabrication of the yet-to-be-named material, $80GeSe_2$-$18Ga_2Se_3$, were outlined. The second approach makes use of wave-front coding—see Fig. 52. A combined amplitude/phase filter mask introduces a controlled distortion of the transmitted wave-front. A well-designed

Table I Effects on design SWaP-C by using glass and polymer aspheres.

Lens form	Impact on system	SWaP-C effect
No aspheres, all glass	Max number of elements	+S, +W, +C, -P
Addition of aspheres	Fewer elements, shorter track	-S, -W, +P
Addition of polymer aspheres	Less Weight, Less cost	-S, -W, -C

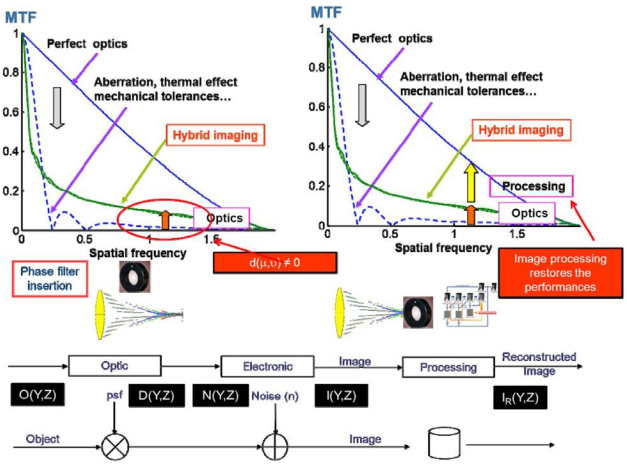

Fig. 52 Wave-front and image processing principles.

filter will lessen the impacts of focus-related aberrations. Post-processing is used to recover the image quality.

One company discussed the impact of using pixel pitches equaling the wavelength of the imaged radiation, on the optics design. It was pointed out that the traditional design approach will quickly increase the number of elements to 3 or more when LW pixel pitch is reduced from 17 μm to 12 μm. It was concluded that in order to achieve low system costs, the future development of lenses for high resolution 12 μm detectors will need to employ image improvement techniques such as wave-front coding.

The manufacture of wafer level chalcogenide arrays is a new technology driven by the recent interest in wafer level thermal cameras. The development and implementation of wafer level packaging for commercial microbolometers has opened the pathway towards full wafer-based thermal imaging systems. The next challenge in development is moving from discrete element LWIR imaging systems to a wafer based optical system, similar to lens assemblies found in cell phone cameras. One paper compared a typical high volume thermal imaging design manufactured from discrete lens elements to a similar design optimized for manufacture through a wafer based approach. Both performance and cost trade-offs were reviewed and discussed.

The use of wafer-level optics was also investigated and presented by a team consisting of representatives from industry and governmental laboratories. A compact MWIR cryogenically cooled multichannel camera in which the optics is merged with the detector, was discussed. Due to the cooling of the optics a very low NEΔT was achieved. Using a post-processing algorithm a well-sampled image was created from a set of under-sampled raw sub-images. The resulting camera has a 4.1 mm track length and 120 ° FOV. Among other new IR optics developments, the following should be noted:

- Increasing the LWIR transmittance of Si windows from 50% to over 80% by use of NiO AR coating and annealing.
- A wave-front sensor using a Quadri-Wave Lateral Shearing Interferometer (QWLSI) for characterizing optical components in a way that complements or replaces MTF measurement—see Fig. 53.
- Presentation of a new measurement system which enables characterization of alignment of all individual elements of an IR lens assembly in a non-contact fashion.
- Combining an Echelle spectrograph with an IR camera in order to measure the dielectric coating thickness of thin film coatings.
- Achieving a spectral transmission range from UV to 7 μm for ZBLAN fibers by processing under controlled microgravity conditions during a parabolic flight.

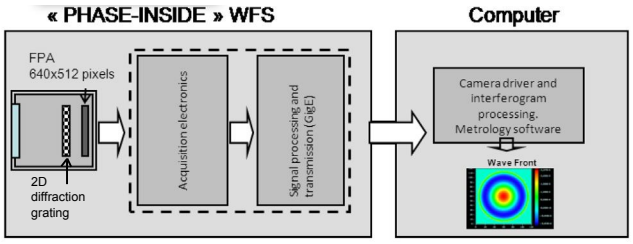

Fig. 53 Schematic of the "Phase Inside" wave front sensor. The incoming light goes through a two-dimensional grating prior to being detected by a focal plane array. The FPA output is converted to digital and signal processed before being sent to a computer for processing the interferogram showing the wave front.

Smart Processing

This session primarily covers advances in detector readout technology that include functionality beyond simple signal/image acquisition.

The first paper in this session considered the evolution of the video output signal from thermal imagers, going back to World War II. Issues for new systems that utilize a million pixels or more were included.

The nonuniformity correction of uncooled FPAs that is computationally-based and includes the influence of optics was discussed and compared to the traditional method of using a camera shutter. Fig. 54 shows how the two methods compare.

The benefits of over-sampling in image sensors were presented in a paper that used the example of false alarm suppression as illustrated in Fig. 55.

A novel readout circuit having the ability to select between two distinct types of input circuits—source-follower and CTIA—for high- and low-level flux conditions, respectively was presented. The readout design was specifically targeted for SWIR detectors, but may have usefulness for dual-band detectors as well.

Digital implementation of a time-delay-and-integration (TDI) readout function was the subject of a presentation. Lower power consumption was claimed, compared to an analog equivalent.

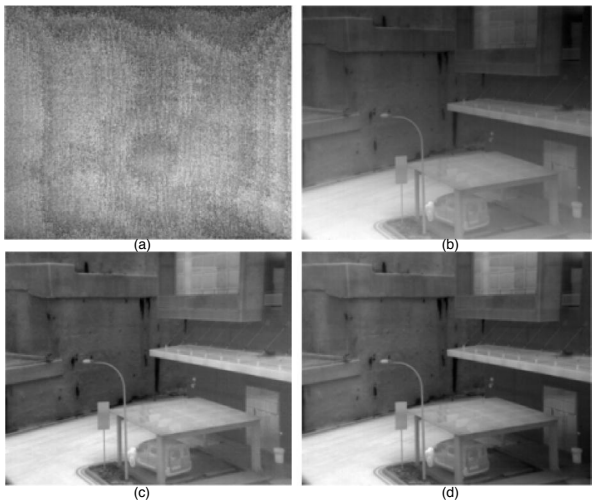

Fig. 54 Comparison of NUC methods: (a) exhibits the raw images, (b) shows the results after FPA NUC, (c) after both FPA and optics NUC, and (d) the results for standard shutter-based NUC.

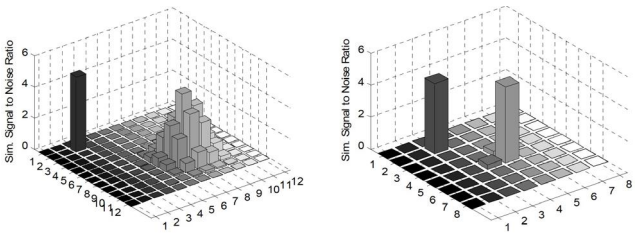

Fig. 55 Over-sampled pixels illustrate realistic blur from the PSF and can identify single point noise spike as a false alarm (left), while under-sampled imager (right) has a near single pixel real target and single pixel noise spike which cannot easily be distinguished.

A readout with a CTIA input and low noise—~5 electrons—for SWIR imaging was given. A sample image from a camera using this 640 × 512 readout with 15 μm pitch unit cells is shown in Fig. 56.

A new type of digital readout was reported with reduced quantization noise. Fig. 57 shows the circuit schematic overview. Quantization noise less than 200 e^- is claimed with a charge handling capacity of 2.3 × 10^9 electrons.

Fig. 56 A SWIR image obtained from a camera using a CTIA ROIC hybridized with an InGaAs detector array.

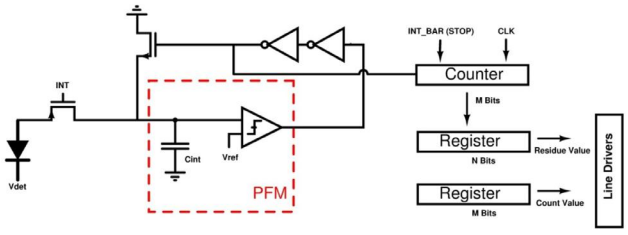

Fig. 57 Block diagram of the proposed digital readout unit cell circuit with reduced quantization noise.

Applications

Presentations focusing on applications of the various infrared technologies in systems and subsystems were presented in Oral Sessions 2, 3, 4, 5, and in the Poster Session. As applications are the main drivers for technology R&D, references to system applications can be found throughout the Proceedings.

Infrared in Future Soldier Systems

Future Soldier Systems programs are being implemented in over 25 countries. Presentations at this conference were made describing some of the EO/IR components in the German IdZ (Gladius) program and the Italian Soldato Futuro program.

The German WBZG clip-on sight (HuntIR Mk2) makes use of a HOT 640 × 512 15 μm HgCdTe FPA which is cooled by a specially-designed single-piston linear Stirling cryocooler. The FPA operates at 140 K and the cryocooler has a 25,000 h lifetime. A comparison of this sight with the previous version is shown in Fig. 58.

The Italian Mini Sight 320 makes use of a 320 × 240 uncooled microbolometer (17 μm pixels) and a visible light camera. It is usable as either a pocket scope or mounted on a weapon and weighs less than 330 grams—see Fig. 59.

A new camouflage technology has the potential to reduce the signature of troops and vehicles significantly, thus making the use of infrared sights less effective. Fig. 60 shows the effectiveness of the technology.

Fig. 58 Comparison of the HuntIR Mk2 sight (1.9 kg) compared to the precious version (3.4 kg).

Fig. 59 Soldato Futuro Mini Sight 320.

Fig. 60 Without and with infrared camouflage.

Army Infrared R&D I and II

Several presentations were addressing the detection from moving vehicles of hostile fire threats ranging from small arms to guided missiles. The ultimate goal is to utilize the launch flash or missile propulsion plume in a multi-spectral passive detection methodology that has a low Size, Weight, Power and Cost (SWaP-C).

The flash detection section opened with a discussion of the optimal spectral bands for detection of threats at short and medium ranges. It was indicated how SWIR-NIR-VIS multi-band low cost and low complexity detection means may provide for an optimal technical solution. Following this analysis, a fourth generation SWIR-VIS passive uncooled optical threat locater—see Fig. 61—was presented. Good situational awareness was achieved by using an FPA with a high number of pixels together with a low number of

Fig. 61 Typical installation of the SWIR-VIS system on an armoured personnel carrier.

sensor heads. An optional inclusion of a radar, adding a range capability to the system, was outlined.

A governmental laboratory presented a dual band, passive, uncooled, wide FOV based muzzle flash detection system operating in the NIR spectrum—see Fig. 62. The system was designed using a novel dichroic beam splitter and dual band-pass filter configuration that create two side-by-side images of a scene on a single sensor, thus obtaining good spatial registration between the two bands.

A third sensor module for hostile fire detection at up to long ranges was presented. It was designed for single band MWIR operation at a maximum frame rate of 6500 fps. Fig. 63 shows the difference between two frames, 297 μsec apart, of a .22 caliber rifle round.

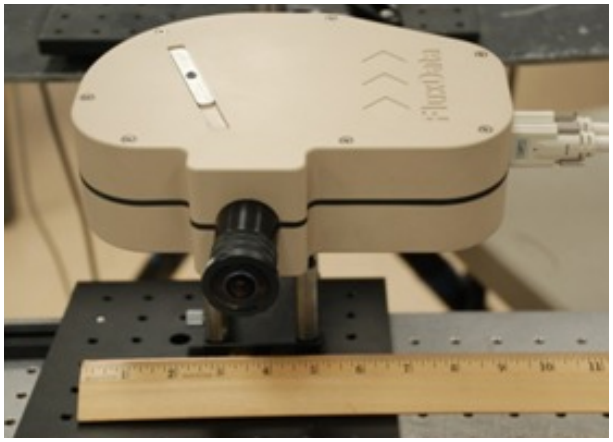

Fig. 62 Wide angle NIR dual band sensor head.

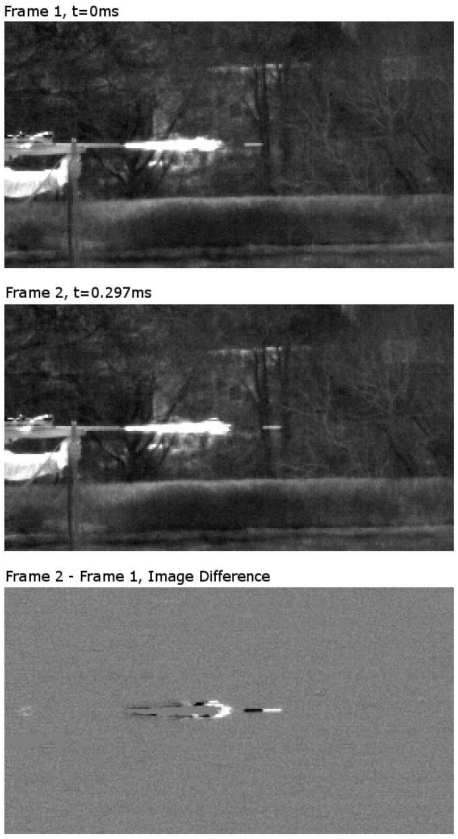

Fig. 63 Two frames 0.3 msec apart of a .22 caliber rifle round and the difference image.

Army vehicles, as well as their mounted infrared sensors, are frequently being upgraded in order to answer new battlefield performance requirements. A flexible approach for the optical concept of a tank thermal sight was outlined. The approach, which uses a varying number of mirrors, facilitates the integration of the sight into upgraded tanks having different available space requirements.

Improved situational awareness is gaining importance and lessons learned from integrations of infrared sensors on armored vehicles, unarmored military vehicles and commercial automobiles were discussed. Each of the applications—close-in and far range situational awareness, as well as drivers vision enhancement, ISR (Intelligence, Surveillance and Reconnaissance) and target designation—has different requirements and challenges. These were detailed and analyzed in the presentation—see Table II.

Table II Typical requirements for wheeled vehicle IR sensors.

Requirement	Human Drivers Aid	Autonomous Vehicle	Situational Awareness	ISR	Targeting
FOV	40 to 60 degrees, fixed.	40 to 60 degrees fixed, zoom optional	180 to 360 degrees fixed	2 degrees to 30, Zoom	1 to 30 degrees in multiple steps
Bandpass	LWIR	Visible and LWIR	Visible and LWIR	Visible, SWIR and MWIR	Visible and MWIR min, with optional SWIR and LWIR.
NEDT	<70 mK	<40 mK	<60 mK	<30 Mk	<25 mK
Laser Rangefinder	No	Yes	No	Yes	Yes
MTBF	>15,000 hours	>10,000 hours	>5000 Hours	>1500 hours	>1000 hours
Cost Sensitivity	High	Moderate now, high in the future	Moderate	Moderate to Low	Low
Weight	<2 Kg	<5Kg	<5Kg	Typically less than 30Kg	Typically less than 50Kg
# of dimensions to the imagery	Two, but three preferred	Two, but three preferred	Two , but three preferred	One	One

Several enabling technologies, having a dominating impact on applications like those covered in the above sections, were discussed. Among these were:

- State-of-the-art 640 × 512, 15 µm pitch detector modules optimized for specific key requirements on system level, such as detector-dewar length for gimbal applications, and size, weight and power reduction for UAVs.

- Megapixel FPAs for both MWIR and LWIR bands with 15 µm pitch for applications like rotorcraft pilotage, persistent surveillance and determination of threat level in personnel targets.

- High Operating Temperature modules with cryocoolers having reduced SWaP and increased reliability, life-time and aural stealth. These characteristics are very attractive for handheld or sniper applications like clip-on for thermal weapon sights.

- Decreasing pixel pitch leading to longer identification ranges and higher compactness. Fig. 64 shows existing and predicted future pixel pitch reduction trends from one major detector developer.

- Use of active e-APD MCT detector for amplification of photo-electrons in order to avoid photon starvation for small detector pitches in systems with high f-numbers against cold backgrounds.

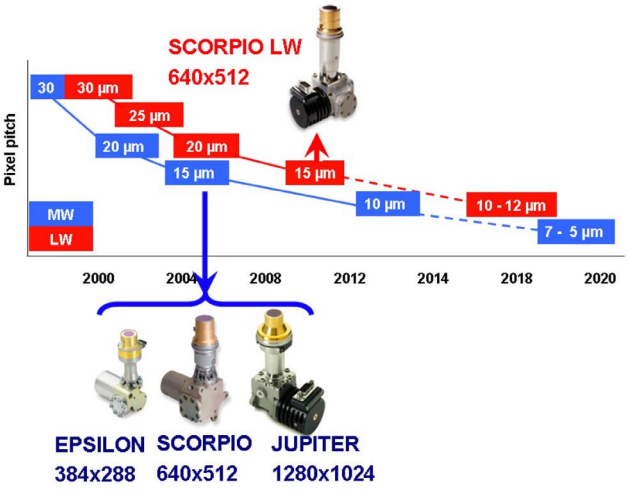

Fig. 64 Pixel pitch reduction trend.

- Decreasing the pixel pitch for MW/LW dual band FPAs in order to enhance target detection and identification ranges in a greater number of battlefield conditions. HDTV resolution with a 12 µm pitch was stated as a future goal.

- Development of detectors covering spectral bands between Vis and VLWIR. The applications range from military to meteorology.

- A novel technology for protection of SWIR cameras against laser threats.

Infrared at Sea, in the Air, and Space

Two presentations outlined concepts for ship-based InfraRed Search and Track (IRST) systems as protection against anti-ship missiles and attacking aircraft from up to very long ranges. Both systems provided panoramic search over 360 degrees azimuth at the high update rates required for operation in high atmospheric scintillation. One configuration employed step-and-stare, by use of continuous scanning of the sensor head and a counter-rotating polygonal drum, while the second configuration achieved full stare (no dead-time) by using large FPAs.

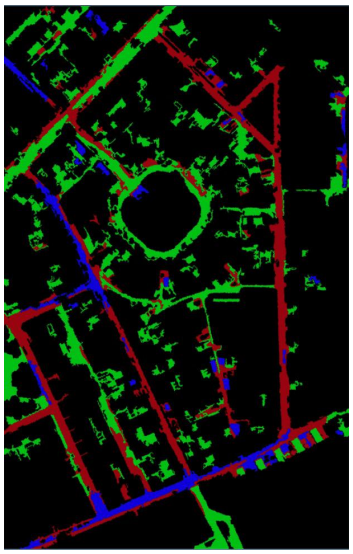

Fig. 65 A road network in the old city of Zeebrugge, characterized by three different types of concrete shown in different colors.

In a follow-up presentation to last year's DUCAS (Detection in Urban scenario using Combined Airborne imaging Sensors) project overview, several examples were presented which showed the successful use of combined hyperspectral and high spatial-resolution data in identifying objects from a suite of airborne sensor-systems. The spectral data contain information pertaining to material qualities. Fig. 65 shows a road network in the old city of Zeebrugge, characterized by three different types of concrete.

One company at the forefront of detector developments presented its advanced FPAs for hyperspectral imaging from air and space. Examples of configurations for airborne and space flight, with and without cryogenic cooling, are shown in Fig 66.

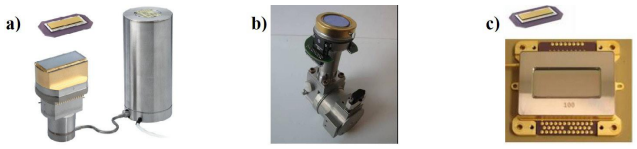

Fig. 66 Neptune and Saturn detectors available configurations : a) airborne configuration of the Saturn detector with a Dewar and a cooler; b) Space configuration of the Neptune detector (500 × 256) with a Dewar and a cooler adapted to space constraints; c) Space configuration of the Saturn detector (1000 × 256) compatible with passive cooling system.

Paul R. Norton

Bjørn F. Andresen

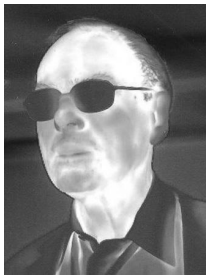

Gabor F. Fulop

Charles Hanson